Combined integral equation formulation and null-field method for the exterior acoustic problem

B. Stupfel, A. Lavie, and J. N. Decarpigny
Laboratoire d'Acoustique, L. A. 253 au CNRS, Institut Supérieur d'Electronique du Nord, 41, Boulevard Vauban, 59046 Lille Cedex, France

(Received 30 August 1987; accepted for publication 8 November 1987)

The numerical implementation of a combined integral equation and null-field method used to solve the exterior Neumann problem [D. S. Jones, Q. J. Mech. Appl. Math. **XXVII**, 129 (1974)] is presented here. The exterior Helmholtz integral equation is solved on the radiating or scattering surface, and the irregular frequencies are eliminated up to a given irregular frequency f_M through the use of M additional null-field equations. An impedance matrix, defined on the object surface, is then obtained that can be used as an exact radiation condition in a finite-element code. The program and the numerical examples presented here are specialized to axisymmetrical problems. A purely null-field method is implemented and simple rules are defined that display its failure when applied to high aspect-ratio objects and (or) in the high-frequency range. Similar, but less restricting, rules are used to specify the numerical limitations of Jones' technique. Besides, a few theoretical considerations clarify the role played by the additional null-field equations in the elimination of the irregular frequencies and help in performing accurate high-frequency computations for surfaces such as the circular cone and the finite circular cylinder.

PACS numbers: 43.20.Rz, 43.20.Tb

INTRODUCTION

The numerical determination of the farfield and/or nearfield pressure in the fluid surrounding an active or passive transducer is one of the major problems in acoustics. It can be solved entirely through the finite-element method (see, e.g., Refs. 1–4). However, if this method is particularly well suited to model the transducer, the structure of which is often complex and composite, the solution of the whole coupled fluid-structure problem, when the overall dimensions of the transducer are large compared with the wavelength of the radiated or scattered waves, involves linear equations systems of large size, the solution of which necessitates the use of powerful computers. The size of these systems can be considerably reduced if the radiation condition is exactly accounted for on the surface of the device through, e.g., an integral equation. This implies the coupling between the finite-element method and an integral equation formulation.

Here, we describe the development of a computer program, solving the three-dimensional Helmholtz equation associated with a prescribed Neumann boundary condition on the radiating or scattering surface S, through a combined integral formulation and null-field method. This program and, consequently, the numerical results presented here, are presently limited to the solution of axially symmetrical problems. One of its important features is that S, as well as the known and unknown functions on S (namely the normal component of the surface velocity and the pressure), are approximated by second-order polynomials, identical to those used in the finite-element code ATILA.[4–6]

The solution of the 3D Helmholtz equation,

$$\Delta p(\mathbf{r}) + k^2 p(\mathbf{r}) = 0, \tag{1}$$

for the pressure $p(\mathbf{r})$ in the infinite domain V_e exterior to S with prescribed boundary conditions on S, is a well-known problem in acoustics and can be performed mainly through the use of three methods (not mentioning the finite-element method): (i) series expansion of $p(\mathbf{r})$ in functions solution of (1) and satisfying the radiation condition, (ii) null-field (or extended boundary condition) method, leading to the T-matrix method for a scattering problem, and (iii) integral equation formulation. The first method is standard when S is a coordinate surface of one of the eleven coordinate systems in which (1) is separable[7]; if not, it is still theoretically justified,[8] independently of the validity of the Rayleigh hypothesis, though it has been very seldomly used.[9] The null-field approach[10] allows the determination of the surface pressure (Neumann conditions) or of the surface normal velocity (Dirichlet conditions). It is widely used in acoustics in the T-matrix formulation to compute the directivity patterns in scattering problems (see, e.g., Refs. 10–14); however, in its usual form, i.e., when spherical wavefunctions [solutions of (1) in the spherical coordinate systems] are used, it is known to be moderately accurate for high aspect-ratio surfaces.[14–16] The integral equation formulation offers two possibilities, depending on the particular integral representation chosen for $p(\mathbf{r})$ (see, e.g., Ref. 17): Either the corresponding integral equation is uniquely solvable on S, or it possesses indeterminate solutions for discrete frequencies, sometimes called irregular frequencies. We do not consider integral representations leading to an integral equation that may have no solution for these frequencies, such as the simple layer representation. For a Neumann boundary problem, the solution of an integral equation of the first type[18–21] is not straightforward since it involves (i) highly singular kernels and (ii) the determination of an unknown surface distribution which,

 0001-4966/88/030927-15$00.80

unlike the pressure, is not necessarily continuous on S. The numerical implementation of an integral equation of the second type is easier (see, e.g., Ref. 22). However, since the number of irregular frequencies increases rapidly with frequency[23] and the numerical solution of the integral equation generates necessarily an indeterminate error, depending on the precision of the computer and the nature of the computation algorithms,[24] it is generally necessary—for medium or high frequency problems—to eliminate these indeterminations. For Neumann boundary conditions, this has been achieved by requiring $p(\mathbf{r})$ to verify one or several additional equations ensuring the unicity of solutions. A good example of this is given by Schenck.[22] He chooses the following integral representation for $p(\mathbf{r})$:

$$p(\mathbf{r}) = \int_S p(\mathbf{r}')\partial n' \, g(\mathbf{r},\mathbf{r}')d\mathbf{r}' - \int_S \partial n' \, p(\mathbf{r}')g(\mathbf{r},\mathbf{r}')d\mathbf{r}', \quad \mathbf{r}\in V_e, \tag{2}$$

the time dependence of the pressure being $e^{-i\omega t}$. Here, $\mathbf{r}$, $\mathbf{r}'$ are arbitrary points, the origin 0 of the coordinate system being chosen anywhere in the interior region V_i, provided it does not belong to S (see Fig. 1); $\mathbf{n}'$ is the unit normal to S at point $\mathbf{r}'$, pointing towards V_e. $g(r,\mathbf{r}') = e^{ik|\mathbf{r}-\mathbf{r}'|}/4\pi|\mathbf{r}-\mathbf{r}'|$ is the free space Green's function ($k = \omega/c$). Here, $\partial n'$ denotes normal differentiation at the point $\mathbf{r}'$ in the direction from V_i towards S and

$$\partial n' \, p(\mathbf{r}') = i\omega\rho v(\mathbf{r}'), \tag{3}$$

where $v(\mathbf{r}')$ is the normal component of the velocity at point $\mathbf{r}'$ and ρ is the fluid density modulus. For a radiation problem, $v(\mathbf{r}')$ is known on S; for a scattering problem, the incident pressure must be added to the right-hand side of (2) and, in the case of a perfectly rigid object, $\partial n' \, p(\mathbf{r}') = 0$ is put in place of (3), p being the total (incident plus scattered) pressure. If $\mathbf{r}$ belongs to S, then we obtain the corresponding "exterior Helmholtz integral equation":

$$\gamma(\mathbf{r})p(\mathbf{r}) = \int_S p(\mathbf{r}')\partial n' \, g(\mathbf{r},\mathbf{r}')d\mathbf{r}' - \int_S \partial n' \, p(\mathbf{r}')g(\mathbf{r},\mathbf{r}')d\mathbf{r}', \quad \mathbf{r}\in S, \tag{4}$$

where $\gamma(\mathbf{r})$ is a surface-dependent coefficient equal to $\frac{1}{2}$ when $\mathbf{r}$ is a regular point on S. If $\mathbf{r}$ belongs to V_i, then the right-hand side of (2) is zero, so that

$$\int_S p(\mathbf{r}')\partial n' \, g(\mathbf{r},\mathbf{r}')d\mathbf{r}' = \int_S \partial n' \, p(\mathbf{r}')g(\mathbf{r},\mathbf{r}')d\mathbf{r}', \quad \mathbf{r}\in V_i. \tag{5}$$

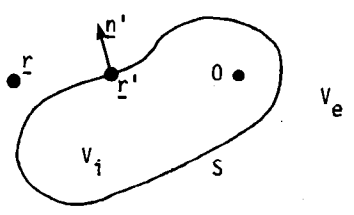

FIG. 1. Geometry and nomenclature. A fluid of density ρ and speed of sound c fills the exterior region V_e.

When f is an irregular frequency, i.e., when $k = 2\pi f/c$ is an eigenvalue of the associated interior Dirichlet problem

$$\Delta\eta(\mathbf{r}) + k^2\eta(\mathbf{r}) = 0, \quad \mathbf{r}\in V_i, \qquad \eta(\mathbf{r}) = 0, \quad \mathbf{r}\in S, \tag{6}$$

then the indeterminate solutions of (4) are of the form $[p(\mathbf{r}) + u(\mathbf{r})]$, where $u(\mathbf{r})$ is defined on S by

$$\gamma(\mathbf{r})u(\mathbf{r}) = \int_S u(\mathbf{r}')\partial n' \, g(\mathbf{r},\mathbf{r}')d\mathbf{r}', \quad \mathbf{r}\in S, \tag{7}$$

and is related to the eigenfunction $\eta(\mathbf{r})$ by

$$\eta(\mathbf{r}) = \int_S u(\mathbf{r}')\partial n' \, g(\mathbf{r},\mathbf{r}')d\mathbf{r}', \quad \mathbf{r}\in V_i. \tag{8}$$

Schenck has shown that if every solution of (4) also satisfies (5) for at least one point $\mathbf{r}$ in V_i, then all the irregular frequencies are suppressed, provided that $\mathbf{r}$ is not situated on a nodal surface of the corresponding eigenfunction $\eta(\mathbf{r})$. However, from a formal point of view, this method presents serious drawbacks since (i) the nodal surfaces are not usually known *a priori*, (ii) their density increases with frequency, and (iii) no rules have been given on how many points should be chosen in V_i and where they should be located. It seems that these points are distributed at random inside V_i so that it is unlikely they all fall on nodal surfaces. For low or moderately high frequencies, this technique is successful.[22,25,26]

Here, we implement numerically another method—though based on the same principles—whose author is D. S. Jones.[27] Jones has established the following result, which we shall afterwards call R1: If $p(\mathbf{r})$ simultaneously satisfies (4) and the set of M^2 null-field equations,

$$\int_S p(\mathbf{r})\partial n \, \Psi_m^n(\mathbf{r})d\mathbf{r} = \int_S \partial n \, p(\mathbf{r})\Psi_m^n(\mathbf{r})d\mathbf{r}, \qquad 0\leqslant m\leqslant M-1, \quad |n|\leqslant m, \tag{9}$$

then the irregular frequencies such that $k\leqslant k_M$ are suppressed, where the eigenvalues of (6) are ordered so that $k_1\leqslant k_2\leqslant\cdots\leqslant k_M\leqslant\cdots$. This condition is sufficient but not necessary. In (9),

$$\Psi_m^n(\mathbf{r}) = h_m(kr)Y_m^{n*}(\theta,\varphi) \tag{10}$$

is an outgoing spherical wave, solution of (1) and satisfying the radiation condition [$\mathbf{r}$ is expressed in spherical coordinates (r,θ,φ)]; $h_m(kr)$ is the spherical Hankel function of order m, behaving like e^{ikr}/r at infinity,

$$h_m(kr) = j_m(kr) + iy_m(kr), \tag{11}$$

where $j_m(kr)$ and $y_m(kr)$ are, respectively, the spherical Bessel and Neumann functions of order m. $Y_m^n(\theta,\varphi)$ is a spherical harmonic (the asterisk denotes the complex conjugate). For an axially symmetrical problem, $n = 0$ and $Y_m^0(\theta)$ is the Legendre polynomial of order m, $P_m(\cos\theta)$. From a formal point of view, the advantage of such a theorem, compared, e.g., to Schenck's method [note that, when $M = 1$, (9) is equivalent to (5) with $\mathbf{r} = 0$] is obvious, especially when associated with the following result[27,28]: If a is the radius of a sphere lying entirely within S, and A the radius of a sphere totally enclosing S, then

$$K_n/A \leqslant k_n \leqslant K_n/a,$$

where K_n is the nth eigenvalue of (6) for a sphere of unit radius. More accurate bounds are obtained when other surfaces are used, approximating S more closely and leaving the calculation of the associated K_n simple. Of course, still better values are obtained for K_n, if a computer program solving (6) and based, e.g., on the finite-element method, is at hand. In fact, in his article, Jones presents two methods in order to suppress the irregular frequencies. We have retained the second one ("an alternative approach"), mainly because the first method introduces coefficients that are not specified, apart from the fact that they must be real and nonzero (note that these coefficients can be chosen so that they are equal to the T-matrix coefficients when the surface pressure is expanded in series of spherical waves.[29,30]) Moreover, the integral representation used in the first method involves the determination of a not necessarily continuous function on S, which may induce some complications in the numerical solution of the corresponding integral equation.

The organization of this article is as follows: Since the additional equations we use are the null-field equations, we have first implemented (Sec. I) a computer program based on the null-field method only. If the approach implemented for this purpose is not new,[31] on the other hand, we give simple rules specifying its numerical efficiency, and depending on the frequency, the number of significant digits used in the computations and on the aspect ratio of S. Numerical examples are given. In Sec. II, we describe the method and computation algorithms implemented for the solution of the integral equation (4) as well as for the solution of the combined integral and null-field equations. Here again, simple rules, similar to those defined in the previous section, are given that specify the numerical limitations of this technique. Besides, a few theoretical considerations enable us to understand more clearly the role played by the null-field equations in the elimination of the irregular frequencies. Section III is devoted to numerical examples illustrating the previous considerations and displaying the efficiency of this combined method, in particular in the high-frequency range.

I. NULL-FIELD METHOD

Let us first review. The null-field equations (9) can be obtained either directly from the application in V_e of the second Green's identity to functions $\Psi_m^n(\mathbf{r})$ and $p(\mathbf{r})$, or from (5): If $\mathbf{r}$ is some point situated inside a sphere S_i of radius R_i and lying entirely within S, then

$$g(\mathbf{r},\mathbf{r}') = ik \sum_{m=0}^{\infty} \sum_{|n|\leqslant m} \Psi_m^n(\mathbf{r}')\bar{\Psi}_m^n(\mathbf{r}), \quad \mathbf{r}'\in S, \quad r < R_i. \tag{12}$$

Here $\bar{\Psi}_m^n(\mathbf{r})$ is the regular spherical wave solution of (1),

$$\bar{\Psi}_m^n(\mathbf{r}) = j_m(kr)\,Y_m^n(\theta,\varphi). \tag{13}$$

Applying (12) into (5), we have, since the Y_m^n are orthogonal,

$$j_m(kr)\int_S p(\mathbf{r}')\partial n'\,\Psi_m^n(\mathbf{r}')d\mathbf{r}' = j_m(kr)\int_S \partial n'\,p(\mathbf{r}')\Psi_m^n(\mathbf{r}')d\mathbf{r}' \tag{14}$$

for all n,m. Finally, if $\mathbf{r}$ is chosen so that kr is not a zero of $j_m(x)$, then we obtain (9) with $M=\infty$. This derivation emphasizes the fact that (5) is nontrivial only if $\mathbf{r}$ does not belong to nodal surfaces—which appear here through the $j_m(kr)$ [see (14)]. The infinite set ($M=\infty$) of null-field equations possesses the important property to be uniquely solvable: If $p(\mathbf{r})$ and $p'(\mathbf{r})$ are solutions of (9) with $M=\infty$, then

$$\int_S [p(\mathbf{r}) - p'(\mathbf{r})]\partial n\,\Psi_m^n(\mathbf{r})d\mathbf{r} = 0, \qquad 0\leqslant m\leqslant\infty, \quad |n|\leqslant m,$$

and the completeness of the infinite set of functions $\{\partial n\,\Psi_m^n\}$ on S[32] ensures that $p(\mathbf{r}) = p'(\mathbf{r})$ almost everywhere on S. The numerical solution of the finite set of simultaneous equations (9) allows the computation of the surface pressure, the accuracy of which increases with M (we shall discuss this point later on). The pressure values in V_e can then be obtained from (2) and, in particular, the directivity pattern $f_0(\theta,\varphi)$,

$$p(\mathbf{r}) \underset{r\to\infty}{\sim} (e^{ikr}/r)f_0(\theta,\varphi) + O(r^{-2}),$$

is given by

$$f_0(\theta,\varphi) = -\frac{ik}{4\pi}\int_S p(\mathbf{r}')\frac{\mathbf{r}\cdot\mathbf{n}'}{r}\exp\left(-ik\frac{\mathbf{r}\cdot\mathbf{r}'}{r}\right)d\mathbf{r}' - \frac{1}{4\pi}\int_S \partial n'\,p(\mathbf{r}')\exp\left(-ik\frac{\mathbf{r}\cdot\mathbf{r}'}{r}\right)d\mathbf{r}'. \tag{15}$$

However, this method presents a severe drawback, directly related to the use of the spherical wavefunctions $\Psi_m^n(\mathbf{r})$: Like the T-matrix method, its numerical efficiency is limited to low or medium aspect-ratio surfaces, i.e., to surfaces the shape of which differ moderately from the inscribed sphere in S. To overcome this difficulty, it would be advisable to use the wavefunction solution of (1) in a coordinate system better suited to the shape of S[33]; but the numerical computation of such functions does not seem to be a simple task, especially when a good numerical accuracy and the use of high-order functions are necessary.

To implement numerically the null-field equations in the case of an axially symmetrical problem, the surface pressure is approximated by $\bar{p}(\mathbf{r})$,

$$\bar{p}(\mathbf{r}) = \sum_{n=0}^{N-1} a_n\varphi_n(\mathbf{r}), \quad \mathbf{r}\in S, \tag{16}$$

where the $\{\varphi_n\}$ constitutes a complete set of functions on S. The set of coefficients a_n is then a solution to the (possibly) overdetermined ($M\geqslant N$) linear system

$$\mathbf{La} = \mathbf{f}, \tag{17a}$$

with

$$L_{mn} = \frac{1}{2\pi}\int_S \partial n\, \Psi_m(\mathbf{r})\varphi_n(\mathbf{r})d\mathbf{r}, \tag{17b}$$

$$0 \leqslant m \leqslant M-1, \quad 0 \leqslant n \leqslant N-1,$$

$$f_m = \frac{1}{2\pi}\int_S \Psi_m(\mathbf{r})\partial n\, p(\mathbf{r})d\mathbf{r}, \tag{17c}$$

where $\Psi_m(\mathbf{r})$ stands from now on for $\Psi_m^0(\mathbf{r})$. The choice of the φ_n determines the numerical efficiency of the method. For example, in the T-matrix method, they are generally chosen to be equal to $\bar{\Psi}_n^0$. However, these functions fail to constitute a complete set on S when k is an eigenvalue of the interior Dirichlet problem.[32] Besides, if a large number of terms are needed in (16) to represent accurately $p(\mathbf{r})$, the number N of terms that can be computed is limited by the smallest number defined on the computer and is strongly kr dependent, since $j_n(kr)$ is a rapidly decreasing function of n for large n;

$$j_n(kr) \underset{n\infty}{\sim} \frac{1}{2n+1}\sqrt{\frac{e}{2}}\left(\frac{kre}{2n+1}\right)^n, \quad kr \lesssim n+\frac{1}{2}.$$

Similarly, if we take $\varphi_n = \Psi_n$, which do constitute a complete set on S,[32] then N is limited by the greatest available number, since

$$y_n(kr) \underset{n\infty}{\sim} -\frac{\sqrt{2e}}{2n+1}\left(\frac{2n+1}{ekr}\right)^{n+1}, \quad kr \lesssim n+\frac{1}{2}. \tag{18}$$

Other choices can be made for φ_n.[13,31] For our part, we found it convenient to take $\varphi_n(r) = \cos n\theta$,[31] the angle θ being defined in Fig. 2.

Having in mind the coupling between the combined integral equation–null-field method presented here, and the finite-element code ATILA, the representation of the axisymmetrical surface S and of the normal velocity component $v(\mathbf{r})$ are those used in ATILA.[4–6] The generating line of S is discretized by a finite set of three-node elements (see Fig. 2): The Cartesian coordinates $(x,0,z)$ of a point $\mathbf{r}$ situated on one of these elements are given in terms of the nodal coordinates $(x_\alpha,0,z_\alpha)$ by

$$x(\zeta) = \sum_{\alpha=1}^{3} N_\alpha(\zeta)x_\alpha, \quad z(\zeta) = \sum_{\alpha=1}^{3} N_\alpha(\zeta)z_\alpha, \tag{19}$$

where ζ is the local coordinate, α is the local node number ($\alpha = 1$, 2, or 3), and $N_\alpha(\zeta)$ are the three-node element interpolation functions

$$\begin{aligned} &N_1(\zeta) = \tfrac{1}{2}\zeta(\zeta-1), \quad N_2(\zeta) = 1-\zeta^2, \\ &N_3(\zeta) = \tfrac{1}{2}\zeta(\zeta+1), \quad -1 \leqslant \zeta \leqslant 1. \end{aligned} \tag{20}$$

Similarly, $v(r)$ is approximated on element j by

$$v_j(\mathbf{r}) = \sum_{\alpha=1}^{3} N_\alpha(\zeta)v_{j\alpha}, \tag{21}$$

where $v_{j\alpha}$ is the value of v at node α on element j. From Eqs. (3) and (17c), we obtain

$$f_m = i\omega\rho \sum_{j=1}^{J}\sum_{\alpha=1}^{3} v_{j\alpha}\int_{-1}^{1} d\zeta\, \Psi_m(\mathbf{r}(\zeta))N_\alpha(\zeta)w_j(\zeta) \tag{22}$$

[on element j, $d\mathbf{r} = 2\pi w_j(\zeta)d\zeta$; J is the total number of elements]. Here, we have taken $N = M$, our computations showing that $M > N$ gives no better results. The linear system (17a) is then inverted using standard techniques.

Used as it stands, the null-field method gives erroneous results for small frequencies and/or large M, owing to the undesirable numerical behavior of $\Psi_m(\mathbf{r})$ for the corresponding values of kr and/or m: If 10^A is the greatest number accepted by the computer, then M cannot be larger than $\bar{M}$ defined by [see Eqs. (17b), (10), and (11)]

$$\sup_{\mathbf{r}\in S} \log|y_{\bar{M}}(kr)| < A. \tag{23}$$

It is, therefore, necessary to use a "renormalization" procedure, such as the one defined in Ref. 31, in order to remove the large term $(2m+1)^{m+1}$ in $y_m(kr)$ and to minimize the variations of $r^{-(m+1)}$ along S [see (18)]. Thus for $m \geqslant \bar{M}$, we have replaced $h_m(kr)$ by $\bar{h}_m(kr)$:

$$\begin{aligned} &\bar{h}_m(kr) = i\,\bar{y}_m(kr), \\ &y_m(kr) = \frac{\sqrt{2e}}{2m+1}\left(\frac{2m+1}{ek\bar{r}}\right)^{m+1}\bar{y}_m(kr), \end{aligned} \tag{24}$$

where $r_{\min} \leqslant \bar{r} \leqslant r_{\max}$, $r_{\min}$ and $r_{\max}$ being the minimum and maximum values of r, $\mathbf{r} \in S$. Unlike the authors of Ref. 31, we did not use an asymptotic expression of $y_m(x)$ to evaluate $\bar{y}_m(x)$, for a good numerical accuracy is necessary when dealing with the null-field method. For $kr > 0.1$ the $\bar{y}_m$ are computed through ascending recursion:

$$\begin{aligned} \bar{y}_0(kr) &= -\cos(kr)(\bar{r}/r)\sqrt{e/2}, \\ \bar{y}_1(kr) &= -\frac{e^2}{3\sqrt{2e}}\left[\cos kr\left(\frac{\bar{r}}{r}\right)^2 + \frac{k\bar{r}^2}{r}\sin kr\right], \\ \bar{y}_{m+1}(kr) &= e\left(\frac{2m+1}{2m+3}\right)^{m+1}\frac{\bar{r}}{r}\bar{y}_m(kr) \\ &\quad - \frac{(ek\bar{r})^2}{(2m-1)(2m+3)}\left(\frac{2m-1}{2m+3}\right)^m \\ &\quad \times \bar{y}_{m-1}(kr), \end{aligned}$$

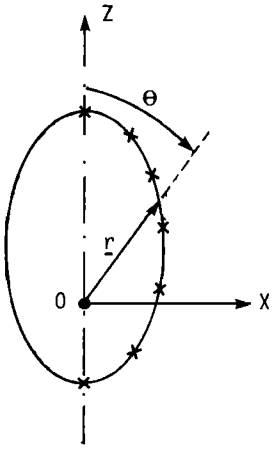

FIG. 2. Definition of the geometry and typical discretization of the generating line of an axisymmetrical body using three-node isoparametric elements.

while, for $kr \leqslant 0.1$,

$$\bar{y}_m = -\frac{2m+1}{\sqrt{2e}}\left(\frac{e}{2m+1}\frac{\bar{r}}{r}\right)^{m+1}(2m-1)!! \times\left(1-\frac{(kr)^2/2}{1!(1-2m)}+\cdots\right),$$

so that the $\bar{y}_m$ are computed with the same accuracy as the y_m. Substituting (24) in (17a)–(17c), and dividing, for $m \geqslant \bar{M}$, (17a) by $[i\sqrt{2e}/(2m+1)][(2m+1)/ek\bar{r}]^{m+1}$, we have

$$\bar{\mathbf{L}}\mathbf{a} = \bar{\mathbf{f}}, \tag{25}$$

with

$$\bar{L}_{mn} = L_{mn}, \quad \bar{f}_m = f_m, \quad m < \bar{M},$$

$$\bar{L}_{mn} = \frac{1}{2\pi}\int_S \left\{\left[\frac{m}{kr}\bar{y}_m(kr) - \frac{2m+1}{ek\bar{r}}\left(\frac{2m+3}{2m+1}\right)^{m+1} \times \bar{y}_{m+1}(kr)\right]\partial n(kr) \times P_m(\cos\theta) + \bar{y}_m(kr)\partial n\, P_m(\cos\theta)\right\}\varphi_n(\theta)d\mathbf{r}, \quad m \geqslant \bar{M}, \tag{26}$$

$$\bar{f}_m = \frac{1}{2\pi}\int_S d\mathbf{r}\,\partial n\, p(\mathbf{r})P_m(\cos\theta)\bar{y}_m(kr), \quad m \geqslant \bar{M}.$$

Since, from (24) and (18),

$$|\bar{y}_m(kr)| \underset{m\infty}{\sim} (\bar{r}/r)^{m+1}, \quad kr \leqslant kr_{\max} \lesssim m + \tfrac{1}{2},$$

and the smallest and greatest numbers accepted by the computer are 10^{-A} and 10^{A}, the greatest value M can achieve must verify

$$(M+1)\log(\bar{r}/r_{\max}) \gtrsim -A, \quad (M+1)\log(\bar{r}/r_{\min}) \lesssim A.$$

If $\bar{r}$ is chosen so that these inequalities are optimized for M, then $\bar{r} = \sqrt{r_{\max} r_{\min}}$ and

$$M + 1 \lesssim \frac{2A}{\log(r_{\max}/r_{\min})}. \tag{27}$$

However, even if M satisfies (27), numerical computations show that the improved null-field method described above still fails in some cases to give the correct surface pressure, especially for high-aspect-ratio objects, i.e., when $r_{\max}/r_{\min}$ is large. Careful investigations have shown that this failure is due to a loss of numerical accuracy in the computations of L_{mn} and f_m. In fact, from (17b), (17c), (10), and (11), it is easy to see that the variations of $y_m(kr)$, which determine the behavior of $h_m(kr)$ for large m, must not be too important on S. More precisely, if P is the number of significant digits taken into account in the numerical computation, M must verify, for M sufficiently large,

$$\log|y_M(kr_{\min})/y_M(kr_{\max})| \lesssim P. \tag{28}$$

Using (18), we then obtain the simple inequality

$$(M+1)\log E \lesssim P, \quad E = r_{\max}/r_{\min},$$
$$kr_{\max} \lesssim M + \tfrac{1}{2}. \tag{29}$$

If $kr_{\max}$ is not smaller than $(M+\frac{1}{2})$, then another asymptotic expression must be used for $y_m(kr)$ in place of (18). We have thoroughly verified, through numerous computations made on various surfaces, that (29) [or (28)] indeed gives a reliable largest value for M. Comparing (27) and (29), we see that, since $P < A$, (29) is the dominant inequality.

In order to evaluate the ability of the null-field method to compute $p(S)$ and, hence, to solve the Helmholtz equation, we must further try to estimate the values of M and N, the number of null-field equations and of Fourier coefficients to be taken into account in order to compute $p(S)$ with good accuracy. This is indeed a difficult task and, to our knowledge, no answer to this problem has been given till now. Intuitively, we expect N and M to be increasing functions of k, as corroborated by the numerical computations. In fact, we show in the following discussion, from simple arguments, that M must be greater than kr in order to compute $p(\mathbf{r})$ with some accuracy at point $\mathbf{r}$ on S. If $\bar{p}(\mathbf{r})$ is the approximate solution of (9) and $p(\mathbf{r})$ the exact solution ($M = \infty$), then

$$\int_S \epsilon(\mathbf{r})\partial n\, \Psi_{M-1}(\mathbf{r})d\mathbf{r} = 0, \tag{30}$$

where $\epsilon(r) = p(\mathbf{r}) - \bar{p}(\mathbf{r})$ is the absolute error on S. Now, if M is sufficiently large so that (18) is valid, then

$$\partial n\, \Psi_{M-1}(\mathbf{r}) \underset{M\infty}{\sim} \frac{-i\sqrt{2e}}{2(2M+1)} P_{M-1}(\cos\theta) \times\left(\frac{2M+1}{ekr}\right)^{M+1}\partial n(kr), \tag{31}$$

and the maximum value of $\partial n\, \Psi_{M-1}(\mathbf{r})$ is reached for $r = r_{\min}$ or in the immediate vicinity of $r_{\min}$ (the Legendre polynomial must not be zero for the corresponding value of the angle θ). Hence, on the part Δ of S defined by $r \in [r_{\min} - \delta,\ r_{\min} + \delta]$, $\delta > 0$, $\partial n\, \Psi_{M-1}(\mathbf{r})$ reaches very large values. This implies that, for $\mathbf{r} \in \Delta$, $\epsilon(\mathbf{r})$ must be very small in order that (30) is verified. Moreover, (31) shows that for large M, the size of Δ is an increasing function of M and a decreasing function of k: This means (i) that the part of the surface S on which $p(\mathbf{r})$ is accurately computed starts at $r = r_{\min}$ and enlarges with increasing M, and (ii) the value of M from which Δ occurs increases with frequency (see Appendix A). To be more precise, it is necessary for kr to be smaller than the first zero of $y_m(kr)$ in order for (31) to be verified, i.e., $kr < M$: If convergence is wished on the whole surface, then

$$kr_{\max} < M. \tag{32}$$

Of course, this is not a mathematical proof, and the inequality (32) is certainly a rough estimate of the minimum value to be given to M in order that convergence is achieved for $p(S)$. But the crude arguments given above explain very satisfactorily the overall behavior of the null-field method displayed by the numerical experiments, as we shall see later on. The fact that, for sufficiently large M, the surface pressure is accurately computed in a zone near the origin has already been noted,[34] and suggests that $p(S)$ may be calculated by parts, the origin being moved for each calculation.

Summing up these results, the simple inequalities

$$kr_{\max} < M \lesssim M_p = P/\log E - 1, \quad kr_{\max} \lesssim M + \tfrac{1}{2} \tag{33}$$

may help to define the range of application of the null-field method described in this work: If the inequality $kr_{\max} \lesssim M + \frac{1}{2}$ is not verified, then the right-hand side inequality of (33) must be replaced by (28). Equation (33) shows clearly that this method is less numerically efficient in the high-frequency range and/or for high aspect-ratio objects. Of course, the origin must be chosen in order to minimize E.

Before presenting some numerical results, here we briefly expose a few theoretical considerations that may help to give a better understanding of the null-field method. Since the $\{\partial n\, \Psi_m\}$ constitutes a linearly independent and complete set on S,[29,30] there exists a set of uniquely defined functions $\{\chi_p\}$, orthogonal to the set $\{\partial n\, \Psi_m\}$ and also linearly independent and complete on S. If $\chi_p(\mathbf{r})$ is approximated by

$$\bar{\chi}_p(\mathbf{r}) = \sum_{n=0}^{N-1} \alpha_{np} \varphi_n(\mathbf{r}), \quad \mathbf{r} \in S, \tag{34}$$

where $\bar{\chi}_p$ is so defined as to verify

$$\int_S \bar{\chi}_p(\mathbf{r}) \partial n\, \Psi_m(\mathbf{r}) d\mathbf{r} = \delta_{mp}, \tag{35}$$

then, with $M = N$,

$$\alpha = \mathsf{L}^{-1}. \tag{36}$$

Moreover, it is easy to show, using (35), that the series expansion on the set $\{\bar{\chi}_p\}$ of $\bar{p}(\mathbf{r})$, defined by (16) and verifying (9), is

$$\bar{p}(\mathbf{r}) = \sum_{p=0}^{N-1} f_p \bar{\chi}_p(\mathbf{r}), \tag{37}$$

and f_p has been defined by (17c). Hence, the null-field method can be considered as a technique allowing the (approximate) computation of the set $\{\chi_p\}$ [see (34) and (36)]. We see at once that if the φ_n differ from the generally unknown χ_p, then L is not diagonal and the coefficients α are M dependent ($M = N$ here). Thus the error in the computation of $p(S)$ comes from the fact that (i) the series in (34) and (37) are truncated, and (ii) the α_{np} are only approximately determined. Since both χ_p and $\bar{\chi}_p$ satisfy (35) for $p = 0, \ldots, M-1$, then $\epsilon_p(\mathbf{r}) = \chi_p(\mathbf{r}) - \bar{\chi}_p(\mathbf{r})$, $\mathbf{r} \in S$, verify (30), and the arguments used to evaluate $p(S) - \bar{p}(S)$ show that, for a sufficiently large M, $\epsilon_p(\mathbf{r})$ will be all the smaller as $\mathbf{r}$ is near the origin.

Now we present numerical calculations performed in order to check the method presented here as well as to illustrate and verify the various assertions mentioned previously. All the computations were performed in double precision on an IBM 4341 model 2, so that $A = 76$ and $P = 17$. We used the point source check throughout[22,26]: Point source of unitary amplitude is situated at the origin of the coordinate system; the value $v_{j\alpha}$ of v [see (21)] is computed exactly at node α on element j, and the $\{v_{j\alpha}\}$ are fed as data in the computer. The calculated $\bar{p}(S)$ is then compared to the exact pressure $p(\mathbf{r}) = e^{ikr}/r$, $\mathbf{r} \in S$. The computations were performed on two circular cylinders of radius a and height $2b$ (Figs. 3–5) and on a cone of height $h = 3$ with a circular cross section of radius $a = 1.5$ (Fig. 6). When the problem admits a symmetry plane normal to the revolution axis $0z$, then the only nontrivial null-field equations are those for which m is even,

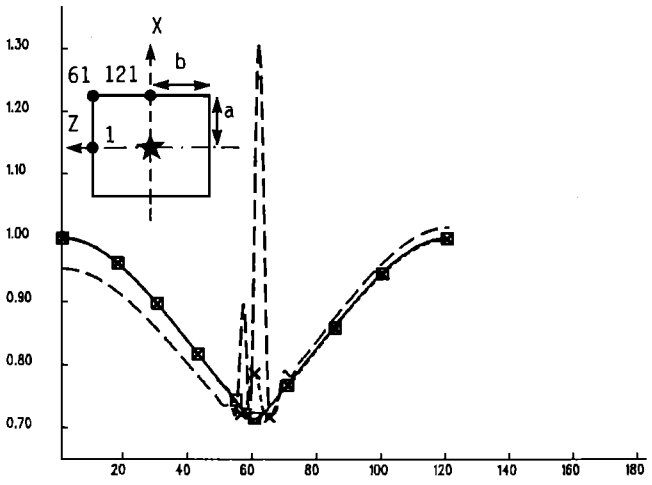

FIG. 3. The modulus of the surface pressure $|p(\mathbf{r})|$ as a function of the position of the surface point $\mathbf{r}$ indicated by its node number for a surface normal velocity distribution corresponding to a point source located at the center of symmetry. The nodes numbering is given on the surface sketch. Z is the revolution axis. Cylinder: $a = 1$, $b = 1$; $k = 1$. — exact $|p(\mathbf{r})| = 1/r$; -⊟- computed $|\bar{p}(\mathbf{r})|$ with $M = 119$; --×-- $|\bar{p}(\mathbf{r})|$ with $M = 149$; — — — $|\bar{p}(\mathbf{r})|$ with $M = 159$.

and the Fourier coefficients with odd indexes are zero. In each figure, the variations of $|p(\mathbf{r})| = r^{-1}$ and $|\bar{p}(\mathbf{r})|$ are represented—this last quantity being computed for different values of M—with $\mathbf{r}$ located on S; the position of $\mathbf{r}$ is identified by the number of the corresponding node (the numbering of nodes is given in each figure); the location of the point source is indicated by the star and coincides with the origin of the coordinate system. The number of nodes has been taken large enough to ensure a good representation of the exact $v(\mathbf{r})$ and, hence, to minimize the error in the computation of the right-hand side of (9). The values of the parameters relevant to each case are given in Table I. For the low aspect ratio $a = 1$, $b = 1$ cylinder, convergence is achieved for $M \gtrsim 40$ and the best results are obtained for $M \simeq 119$

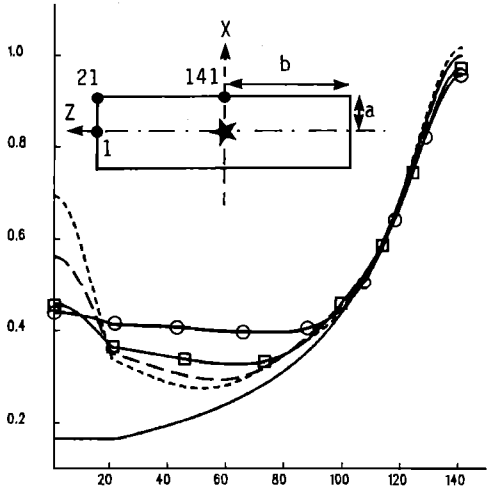

FIG. 4. Same as Fig. 3. Cylinder: $a = 1$, $b = 6$; $k = 1$. — $|p(\mathbf{r})| = 1/r$; -⊖- $|\bar{p}(\mathbf{r})|$ with $M = 7$; -⊟- $|\bar{p}(\mathbf{r})|$ with $M = 13$; — — — $|\bar{p}(\mathbf{r})|$ with $M = 19$; - - - $|\bar{p}(\mathbf{r})|$ with $M = 25$.

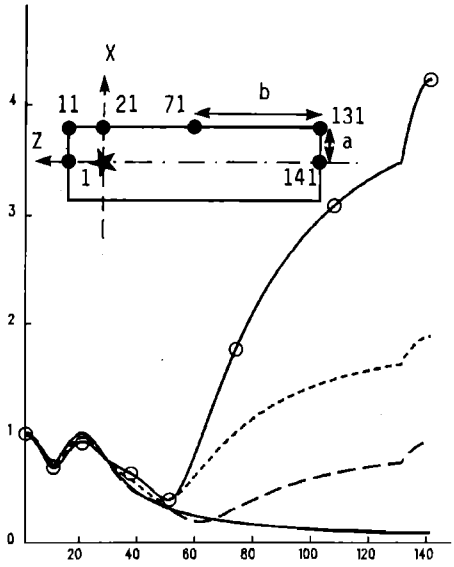

FIG. 5. Same as Fig. 3. Cylinder: $a = 1$, $b = 6$; $k = 1$. The point source and the origin of the coordinate system are located at a distance of 1 from one of the circular faces. — $|p(\mathbf{r})| = 1/r$; - - - $|\bar{p}(\mathbf{r})|$ with $M = 16$; – – – $|\bar{p}(\mathbf{r})|$ with $M = 18$; ⊖ $|\bar{p}(\mathbf{r})|$ with $M = 20$.

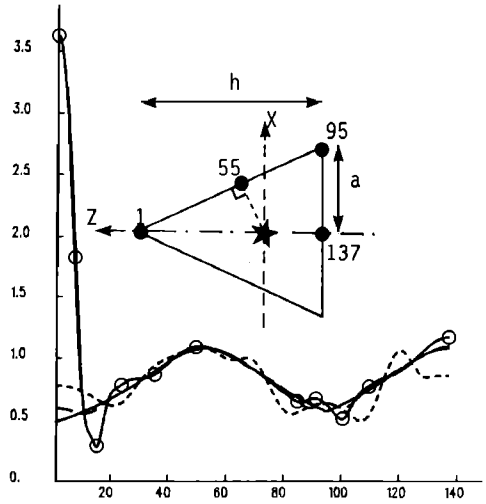

FIG. 6. Same as Fig. 3. Cone: $a = 1.5$, $h = 3$; $k = 5$. The point source and, hence, the origin of the coordinate system are located at a distance of 0.9271 from the circular basis, so that the aspect ratio r_{max}/r_{min} is minimized. — $|p(\mathbf{r})| = 1/r$; - - - $|\bar{p}(\mathbf{r})|$ with $M = 12$; – – – $|\bar{p}(\mathbf{r})|$ with $M = 50$; ⊖ $|\bar{p}(\mathbf{r})|$ with $M = 61$.

(note that the renormalization procedure has been used), whereas accuracy lowers with increasing M, $M \gtrsim 119$, according to (29), and especially in the zone where $r \simeq r_{max}$ (node 61; see Fig. 3). This loss of accuracy occurs in each case (Figs. 3–6) and, when double precision is used, excludes numerical convergence for the $a = 1$, $b = 6$ cylinder and the cone studied here. Figures 4–6 show that, for a sufficiently large M verifying $M \gtrsim kr_{min}$, zone Δ starts at $r = r_{min}$ [there are two equivalent minima for the cone (nodes 55 and 137) and the cylinder of Fig. 5 (nodes 1 and 21)] and spreads with increasing M (see above discussion and Appendix A), provided that $M \lesssim M_P$. Note that (32) is a necessary but not sufficient convergence condition. Figure 5 verifies the fact that $p(S)$ can be computed in part with a change of the coordinate origin. In each case, the overall behaviors of $\mathrm{Re}\,\bar{p}(S)$ and $\mathrm{Im}\,\bar{p}(S)$ are quite similar to the one of $|\bar{p}(S)|$, except, of course, for the frequency-dependent oscillations. The total computing times—independent of the number of nodes—vary from 20 s (Fig. 4, $M = 19$, mirror symmetry is taken into account) to 310 s (Fig. 3, $M = 119$), and are roughly proportional to M^2 (remember that $N = M$) for a given problem.

II. COMBINED INTEGRAL EQUATION AND NULL-FIELD METHOD

First, we describe the implementation of the numerical solution of Eq. (4). We use the same approximations for S and $v(S)$ as those defined in Sec. I [see (19) and (21)], and $p(\mathbf{r})$ is approximated on element j by

$$p_j(\mathbf{r}) = \sum_{\alpha=1}^{3} N_\alpha(\zeta) p_{j\alpha}, \tag{38}$$

where $p_{j\alpha}$ is the unknown value of p at node α on element j. Applying (21) and (38) into Eq. (4) and allowing $\mathbf{r}$ to take the $(2J+1)$ nodal value $\mathbf{r}_{j\alpha}$, we obtain, for $1 \leqslant j \leqslant J$, $1 \leqslant \alpha \leqslant 3$,

$$\gamma(\mathbf{r}_{j\alpha}) p_{j\alpha} = \sum_{l=1}^{J} \sum_{\beta=1}^{3} p_{l\beta} \int_{-1}^{1} d\zeta\, N_\beta(\zeta) w_l(\zeta) A^l_{j\alpha}(\zeta) - i\omega\rho \sum_{l=1}^{J} \sum_{\beta=1}^{3} v_{l\beta} \int_{-1}^{1} d\zeta \times N_\beta(\zeta) w_l(\zeta) B^l_{j\alpha}(\zeta),$$

with

TABLE I. Parameter values relevant to the examples presented on the corresponding figures.

	Location of the point source	E	kr_{min}	kr_{max}	M_p	$\bar{M}$
Figure 3	Center of symmetry	$\sqrt{2}$	1	$\sqrt{2}$	112	47
Figure 4	Center of symmetry	6.08	1	6.08	21	47
Figure 5	$\frac{1}{8}b$ from the center of symmetry	11.05	1	11.05	16	47
Figure 6	$h/3.236$ from the basis	2.24	4.64	10.36	48	72

$$A^l_{j\alpha}(\zeta) = \frac{1}{2\pi}\int_0^{\pi} d\varphi\, h(\zeta,\varphi)\,[\mathbf{r}'(\zeta,\varphi) - \mathbf{r}_{j\alpha}]\cdot\mathbf{n}',$$

$$B^l_{j\alpha}(\zeta) = \frac{1}{2\pi}\int_0^{\pi} d\varphi\, \frac{e^{ikd(\zeta,\varphi)}}{d(\zeta,\varphi)},$$

$$h(\zeta,\varphi) = \frac{e^{ikd(\zeta,\varphi)}}{d^2(\zeta,\varphi)}\left(ik - \frac{1}{d(\zeta,\varphi)}\right),$$

$$d(\zeta,\varphi) = |\mathbf{r}_{j\alpha} - \mathbf{r}'(\zeta,\varphi)|,$$

where $\mathbf{r}'(\zeta,\varphi)$ is situated on element l (φ is the azimuthal angle). Thus Eq. (4) is converted into a $[(2J+1)\times(2J+1)]$ linear system

$$\mathsf{H}\mathbf{p} = \mathsf{D}\mathbf{v}, \tag{39}$$

the solution $\mathbf{p}$ of which is obtained through standard inversion techniques. Here $\gamma(\mathbf{r})$ is given by[35]

$$\gamma(\mathbf{r}) = 1 + \frac{1}{4\pi}\int_S \partial n' \frac{1}{|\mathbf{r}-\mathbf{r}'|}\, d\mathbf{r}',$$

and the integrals are calculated through a Gauss–Legendre quadrature rule, special care being taken for the evaluation of the self-integrals $l = j$ (see Appendix B). To our surprise, and although we worked on our own, the technique presented here in order to solve Eq. (4) was published recently[36] under exactly the same form, except for some very minor details concerning the calculation of self-integrals.

In order to implement Jones' method, the null-field and integral equation programs must be coupled. Concerning the representation of $p(S)$ in the null-field equations, numerical computations show that the Fourier series (16) is much more appropriate than the finite-element interpolation (38). Thus it is necessary to express the a_n in terms of the $p_{j\alpha}$. Since

$$a_n = \frac{2-\delta_{n0}}{\pi}\int_0^{\pi} p(r(\theta))\cos n\theta\, d\theta,$$

we have, from (38),

$$\mathbf{a} = \mathsf{S}\mathbf{p},$$

where S is a $[N\times(2J+1)]$ matrix. Here, N must be sufficiently large to ensure a good representation of $p(S)$ through (16). From (25) and (39), we obtain the following, overdetermined $[(M+2J+1)\times(2J+1)]$, linear system:

$$\sum_{j=1}^{2J+1} H_{ij}p_j = \sum_{j=1}^{2J+1} D_{ij}v_j, \quad 1\leqslant i\leqslant 2J+1,$$

$$\sum_{j=1}^{2J+1} L'_{mj}p_j = \bar{f}_m, \quad 0\leqslant m\leqslant M-1,$$

with

$$L'_{mj} = \sum_{n=0}^{N-1} \bar{L}_{mn}S_{nj}.$$

Finally, a straightforward least-square method leads to the $[(2J+1)\times(2J+1)]$ linear system

$$\mathsf{C}\mathbf{p} = \mathsf{E}\mathbf{v}, \tag{40}$$

which is invertible provided that M is large enough. Thus a matrix impedance $\mathsf{Z} = \mathsf{C}^{-1}\mathsf{E}$ is obtained that can be used as an exact radiation condition for the finite-element code ATILA.

As for the null-field method, $\bar{L}_{mn}$ and $\bar{f}_m$ must be accurately computed and inequalities (27) and (29) [or (28)] still hold, whereas (32) is no longer necessary, so that M is limited here by

$$M \lesssim M_P = P/\log E - 1, \quad kr_{\max} \lesssim M + \tfrac{1}{2}. \tag{41}$$

In the high-frequency range, the number of irregular frequencies can be so large that (41) and Jones' criterion cannot be simultaneously verified. Jones has emphasized[27] that his condition is sufficient but not necessary, the reason being that the nodal surfaces of the M th eigenfunction of (6) divide V_i into *at the most* M subdomains,[37] so that the number of such subdomains can be significantly lower than the order M of the highest irregular frequency situated in the frequency range of interest. Following Jones' proof, this means that the number of efficient null-field equations can be much lower than M. Moreover, we prove in Appendix C the following result (which we shall call afterwards R2) based on a proof of R1 that we think to be more appropriate to his "alternative method" than the one given in Ref. 27 or 38. If, for the M th irregular frequency, $p(S)$ satisfies (4) and (9), then the nodal surfaces of the corresponding eigenfunction, defined by (8) and verifying (6), consist, in the vicinity of the origin chosen for the coordinate system, of a finite number of smooth surfaces, tangent to the cones C_i, loci of the points $\mathbf{r} = (r,\theta,0)$ such as $Y_M(\theta) = 0$; the corresponding statement for nonaxially symmetrical problems is given in Appendix C. This implies that all those eigenfunctions that do not possess this property are necessarily zero and the corresponding irregular frequencies are thus eliminated. By way of illustration, let us consider a sphere S of radius unity: For the third irregular frequency f_3, the eigenfunction of (6) has three nodal surfaces, S and the cones C_1 and C_2, loci of the points $(r,\theta,0)$ so that $Y_2(\theta) = 0$. If R1 is applied, then (9) with $M = 3$ eliminates f_3, wherever the origin 0 of the coordinate system is located. Now, following R2, if 0 does not coincide with the center of S but belongs to C_1 or C_2, then (9) with $M = 2$ is sufficient, whereas, if 0 is not situated on a nodal surface, then (9) with $M = 1$ [or, equivalently, (5) with $\mathbf{r} = 0$] eliminates f_3. Numerical examples presented in Sec. III will verify and further illustrate R2, in particular in the high-frequency range. But, unfortunately, and as far as we are concerned, we do not know to what extent R2 might contradict the general properties of eigenfunctions for a surface S of arbitrary shape, so that we are currently unable—except for simple surfaces such as the sphere or the finite cylinder—to determine (i) the optimal position of the origin and (ii) the exact number of null-field equations to be used.

III. NUMERICAL EXAMPLES

The program is written in simple precision arithmetic for the integral equation part (computation of H and D), whereas the null-field terms (L' and $\mathbf{f}$) are computed in double precision arithmetic in order to have sufficiently large M_P [see (41)]. In most of the numerical examples presented here, the surface velocity distribution is the one of a one-point source (O.P.S.) of strength $+1$ placed at the origin or, in one occasion, of two point sources (T.P.S) of strengths $+1$ and -1 equidistant from the origin and situated on the revolution axis 0z.[22] In each case, due account is taken in the

numerical solution of the problem of a possible symmetry or antisymmetry with respect to the $(x0y)$ plane normal to 0z. It is important to note that, in this case, the only irregular frequencies are those for which the corresponding eigenfunctions are symmetrical or antisymmetrical with respect to $(x0y)$, i.e., are solutions of (6) in that part V_i' of V_i where $z \geqslant 0$, with $\partial n\, \eta(\mathbf{r}) = 0$, $\mathbf{r} \in (x0y)$ (symmetrical case), or $\eta(\mathbf{r}) = 0$, $\mathbf{r} \in (x0y)$ (antisymmetrical case). Since the conditions satisfied by η on the boundary of V_i' are homogeneous, the theorem of Ref. 37 is still applicable and, from the arguments displayed in Appendix C and applied here to the volume V_i', R1 can thus be stated: All the irregular frequencies so that $k \leqslant k_{NE}$ are suppressed if $p(\mathbf{r})$ satisfies (9) with $M = 2NE - 1$ (symmetrical case) or $M = 2NE$ (antisymmetrical case), i.e., if $p(\mathbf{r})$ satisfies NE nontrivial null-field equations. Similar conclusions are obtained when the problem presents other symmetries (antisymmetries) than the mirror symmetry (antisymmetry) considered here.

We have reported in Table II the results of an O.P.S. check performed with no additional equation [system (39) is solved] on the following surfaces: sphere of radius 2, oblate spheroid of semiminor axis 1 and semimajor axis 3, circular cylinder of radius 1 and height 10, and cone of height 3 with a circular basis of radius 1.5. Here, ϵ is defined by

$$\epsilon = \sup_{r \in S} \sqrt{\epsilon_r^2(\mathbf{r}) + \epsilon_i^2(r)} \quad \text{in\%}, \tag{42a}$$

$$\epsilon_r(\mathbf{r}) = \frac{\operatorname{Re} p^c(\mathbf{r}) - \operatorname{Re} p^e(\mathbf{r})}{\sup_{r \in S} \operatorname{Re} p^e(\mathbf{r})}, \tag{42b}$$

$$\epsilon_i(\mathbf{r}) = \frac{\operatorname{Im} p^c(\mathbf{r}) - \operatorname{Im} p^e(\mathbf{r})}{\sup_{r \in S} \operatorname{Im} p^e(\mathbf{r})}, \tag{42c}$$

where p^e and p^c are, respectively, the exact (O.P.S.:e^{ikr}/r) and computed pressures. For these low frequencies, situated well below the first irregular frequency, very good accuracy is obtained with short computing times (less than 13 s). We have represented in Figs. 7 and 8 the variations of ϵ vs k for the $a = 1$, $b = 6$ cylinder ($E = 6.08$) and the $a = 1.5$, $h = 3$ cone ($E = 2.24$) with an O.P.S. located as indicated in Table I. For the cylinder, the eigenvalues of (6) can be calculated analytically and, following R1, we have taken exactly NE nontrivial null-field equations for $k_{NE-1} \leqslant k < k_{NE}$, $NE = 1, \ldots, 7$. For the cone, we have taken $M = 10$ throughout the studied frequency range: The values of the irregular frequencies have been computed from ATILA and agree very well with those obtained from the solution of (39). In this case, we see that accuracy is not lowered when more addi-

TABLE II. Maximum value of the relative error modulus for various surfaces and O.P.S. check: The source is located at the center of symmetry, except for the cone where it is situated at half-height. Here, J is the total number of elements (taking no account of a possible mirror symmetry).

	Sphere $k = 1, J = 16$	Oblate spheroid $k = 1, J = 16$	Cylinder $k = 1, J = 24$	Cone $k = 1, J = 20$
ϵ (%)	0.5	1	0.9	0.9

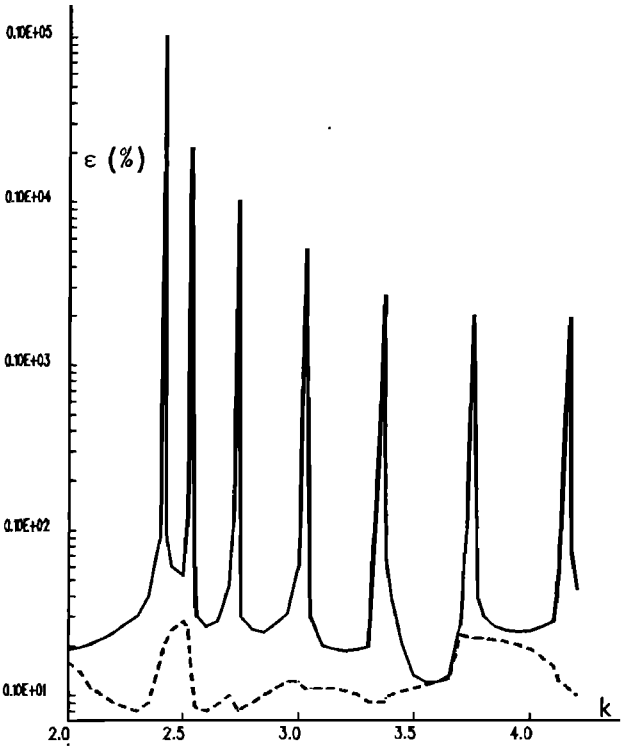

FIG. 7. Maximum value in percent of the modulus of the relative error ϵ (O.P.S.) as a function of the wavenumber k computed for the cylinder $a = 1$, $b = 6$ (see Fig. 4 for a description of the surface geometry and the location of the point source). Equidistant surface mesh obtained with a $\lambda/4$ criterion. — ϵ computed with no additional null-field equations ($NE = 0$); - - - ϵ computed with NE nontrivial null-field equations (see text).

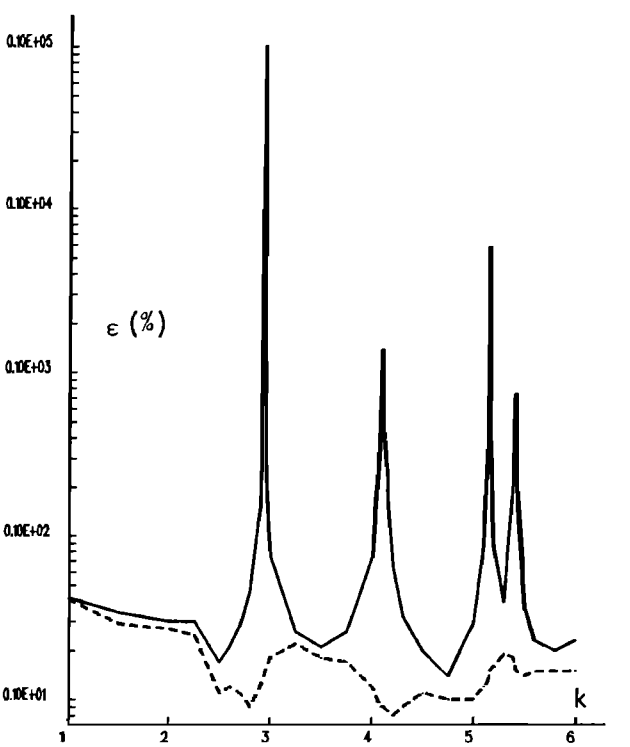

FIG. 8. Same as Fig. 7. Cone $a = 1.5$, $h = 3$ (see Fig. 6). — ϵ with $M = 0$; - - - ϵ with $M = 10$.

tional equations are used than is sufficient, which constitutes an important point when the eigenvalues of (6) are not known *a priori*, and M is then deliberately overestimated. Here, and throughout the following examples, the size of a surface element is taken equal to $\lambda/4$ (λ is the wavelength; the same criterion is taken in ATILA), so that the number of nodes is proportional to f and, therefore, the computing time needed for the calculation of H and D [see (39)] is roughly proportional to f^2. In the low-frequency range, it is obvious that this $\lambda/4$ criterion cannot be valid, as we can verify in Figs. 7 and 8. The computing time needed to implement the null-field equations is roughly proportional to f.M.N. The variations of the exact and computed real and imaginary parts of the pressure on the cylinder and cone surfaces are represented in Figs. 9 and 10 for, respectively, the seventh irregular frequency (T.P.S.: antisymmetrical problem with respect to the $x0y$ plane) and the fourth irregular frequency (O.P.S.), with, respectively, $NE = 0$, 7 ($M = 0$, 14) and $M = 0$, 4. The elimination of the irregular frequencies is clearly displayed. The maximum relative error in the modulus of the directivity pattern $f_0(\theta)$ computed through (15) is 3‰ for the cylinder ($NE = 7$) and 8‰ for the cone ($M = 4$), and the total computing time is, respectively, 260 and 185 s.

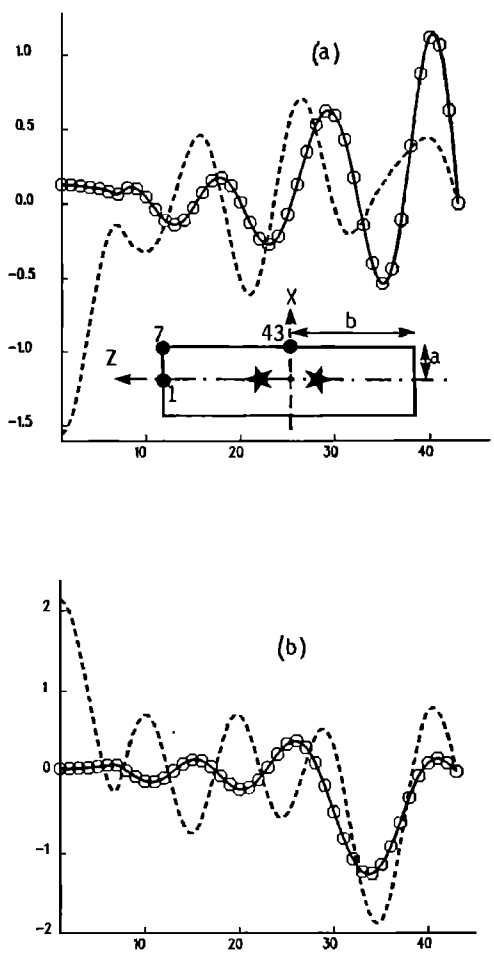

FIG. 9. Surface pressure as a function of the position of the surface point r indicated by its node number for a surface normal velocity corresponding to two point sources of strength + 1 and − 1, the positions of which are indicated by the stars. Cylinder $a = 1$, $b = 6$ (see sketch for the surface geometry and position of nodes), $k = 4.384$ (seventh irregular frequency). The point sources are located at 1.5 from the center of symmetry. Equidistant surface mesh obtained with a $\lambda/4$ criterion. (a) Real part of $p(\mathbf{r})$. (b) Imaginary part of $p(\mathbf{r})$. — exact $p(\mathbf{r})$; - - - computed $p(\mathbf{r})$ with $NE = 0$; -Θ- computed $p(\mathbf{r})$ with $NE = 7$.

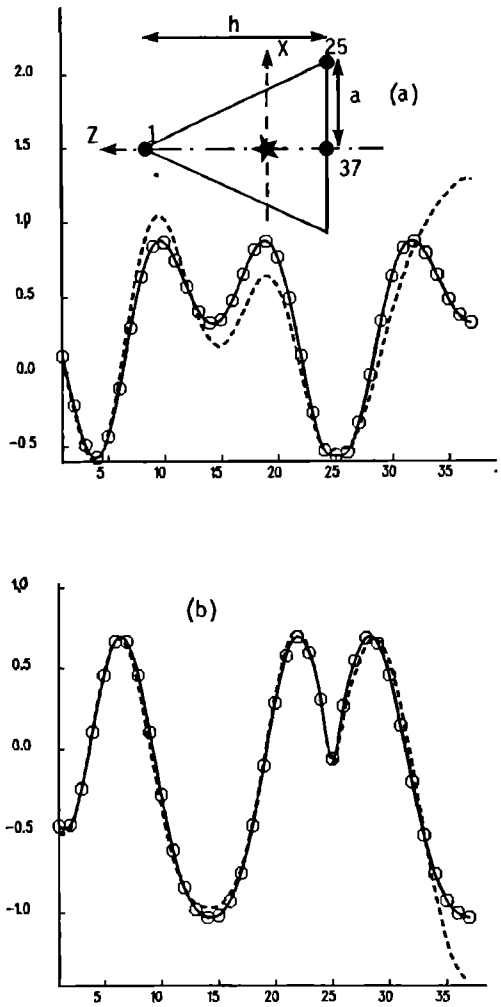

FIG. 10. Same as Fig. 9. O.P.S. check, the source is located as in Fig. 6. Cone: $a = 1.5$, $h = 3$; $k = 5.41$ (fourth irregular frequency). — Exact $p(\mathbf{r})$; - - - computed $p(\mathbf{r})$ with $M = 0$; -Θ- computed $p(\mathbf{r})$ with $M = 4$.

Now we present some numerical results obtained for a sphere of radius unity and relative to the result R2 (see Sec. II). The surface velocity distribution is the one of an O.P.S. placed at the center of the sphere, and the problem is symmetrical with respect to the $x0y$ plane normal to 0z. In this case, the volume V_i' is, e.g., the hemisphere $z \geqslant 0$. We give in Table III, for three irregular frequencies of number NE, the values (in percent) of the maximum relative error ϵ [see (42a)] computed for different values of M. For each of these frequencies, the nodal surfaces of the corresponding eigenfunctions are, in V_i', $S \wedge \{z \geqslant 0\}$ and I conical surfaces intersecting at the origin, loci of the points so that $Y_{2i}(\theta) = 0$, $1 \leqslant i \leqslant I$, $0 \leqslant \theta \leqslant \pi/2$. We see that, except for the second irregular frequency ($NE = 2$), condition R1 ($M = 2NE - 1$) is not necessary, whereas condition R2 ($M = 2I + 1$) is sufficient and necessary, for the implementation of the $(M+1)/2$ nontrivial null-field equations implies, in V_i', $(M+1)/2 = I + 1 > I$ conical nodal surfaces for the corresponding eigenfunctions. If the point source and, consequently, the

TABLE III. Maximum relative error in percent for the pressure computed with $(M+1)/2$ nontrivial null-field equations on the surface of a sphere of radius unity (O.P.S check). Here, k is the wavenumber of the irregular frequency of number NE, and I is the number of the conical nodal surfaces of the corresponding eigenfunction.

k	5.763			10.513				12.791			
NE	2			6				10			
I	1			3				4			
M	0	1	3	0	3	5	7	0	3	7	9
ϵ (%)	150	163	1.7	15	9.1	9.1	1.9	22.8	36.2	37.4	4

origin is moved so that it is not situated on the nodal surfaces, then one null-field equation ($m=0$) is theoretically sufficient to eliminate all the eigenfrequencies. However, numerical computations show that good accuracy is obtained only if the origin is situated far enough from the nodal surfaces. Similar results are obtained for the T.P.S. surface velocity distribution and the circular cylinder.

R2 explains why good results are obtained for computations performed in the high-frequency range even when, owing to (41), R1 is far from being satisfied. We have represented in Fig. 11 the variations of the real and imaginary parts of the exact and computed pressure (O.P.S.) on a $a=1$, $b=12$ cylinder surface of high aspect ratio ($E=12.04$; $M_P=15$) for $NE=0$ and $NE=8$ ($M=14$) and for the 50th irregular frequency; $|f_0(\theta)|$ is calculated with an accuracy better than 1.4%. The total corresponding computing time is 2200 s, 14% of which is devoted to the implementation of the null-field equations. Similar results are obtained for the $a=1.5$, $h=3$ cone (see Fig. 12), finite-element calculations (ATILA) indicating that the computation frequency is situated near the 72nd irregular frequency: The accuracy obtained on $|f_0(\theta)|$ is better than 3%. We present in Fig. 13 numerical results obtained for a cylindrical array ($a=0.2665$ m, $b=0.6295$ m) on which the surface velocity distribution is $v=1$ m/s (radiating zone: hachured part -0.0365 m$\leqslant z\leqslant$0.0365 m) and zero elsewhere. An O.P.S. check performed on this structure gives $\epsilon\leqslant 10.9\%$ ($NE=20$), the error being localized in the vicinity of 0z (see Fig. 14). Note that the computation frequency (30 kHz) stands between the 202nd and 203rd irregular frequencies (respectively 29.96 and 30.014 kHz).

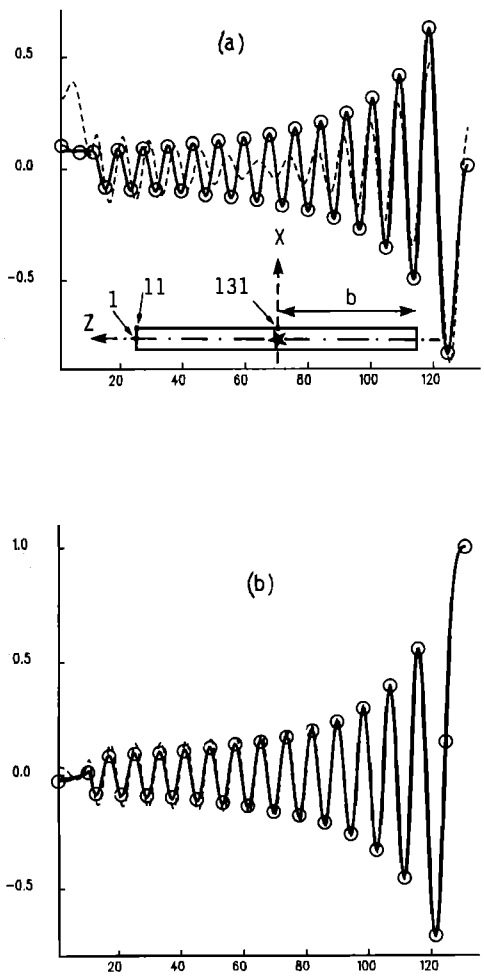

FIG. 11. Same as Fig. 9. O.P.S. check. Cylinder: $a=1$, $b=12$; $k=7.839$ (50th irregular frequency). — exact $p(\mathbf{r})$; - - - computed $p(\mathbf{r})$ with $NE=0$; -⊖- computed $p(\mathbf{r})$ with $NE=8$.

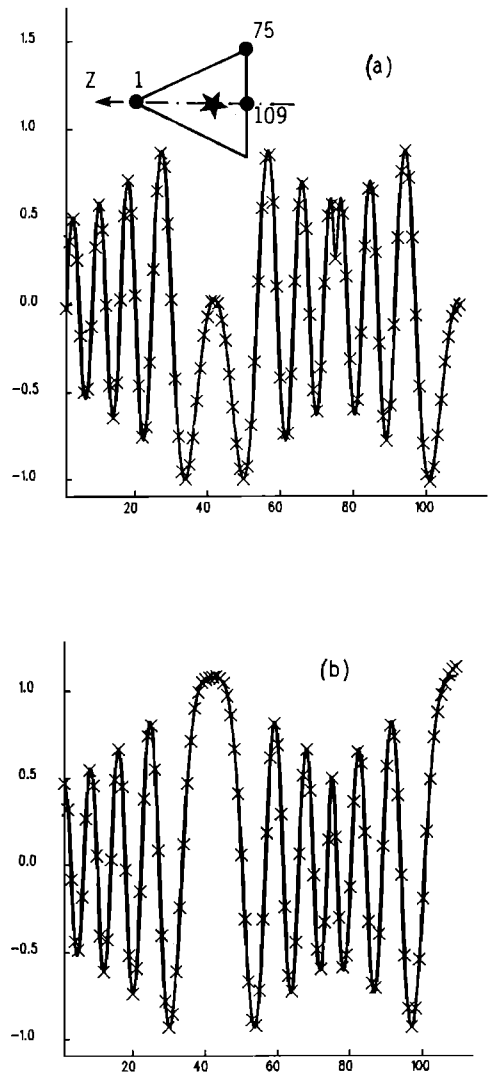

FIG. 12. Same as Fig. 10 for $k=22$. — exact $p(\mathbf{r})$; × computed $p(\mathbf{r})$ with $M=47$.

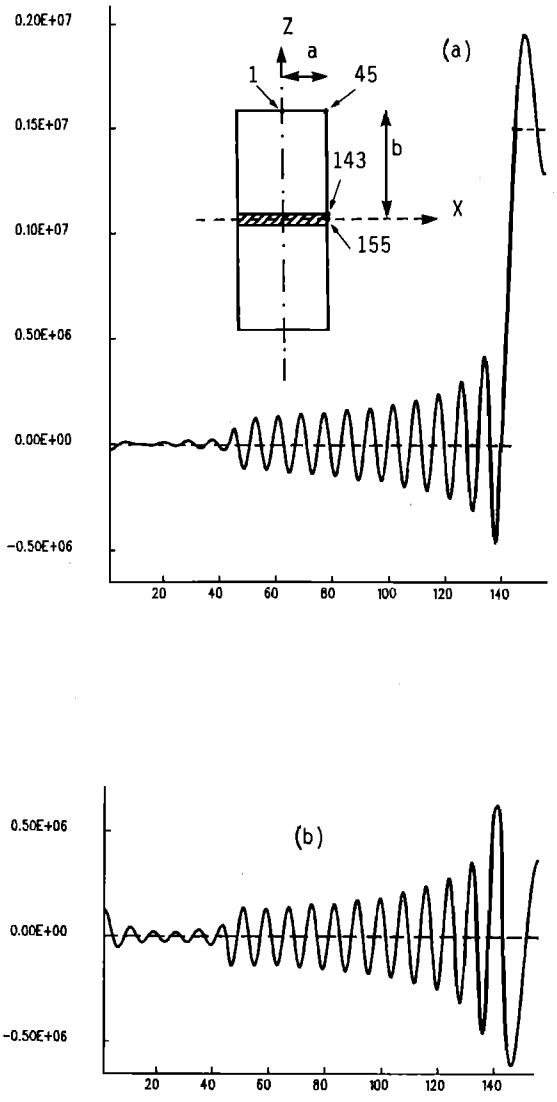

FIG. 13. Same as Fig. 9. Cylinder: $a = 0.2665$ m, $b = 0.6295$ m. $v = 1$ m/s on the hachured part (half-height 0.0365 m) and zero elsewhere. $k = 125.664$ ($f = 30$ kHz). $\rho = 10^3$ kg/m^3 and $c = 1500$ m/s. The surface mesh satisfies the $\lambda/4$ criterion, but its density is increased in the vicinity of and in the radiating zone. — Computed $p(\mathbf{r})$ with $NE = 20$; - - - $p(\mathbf{r}) = \rho c v(\mathbf{r})$.

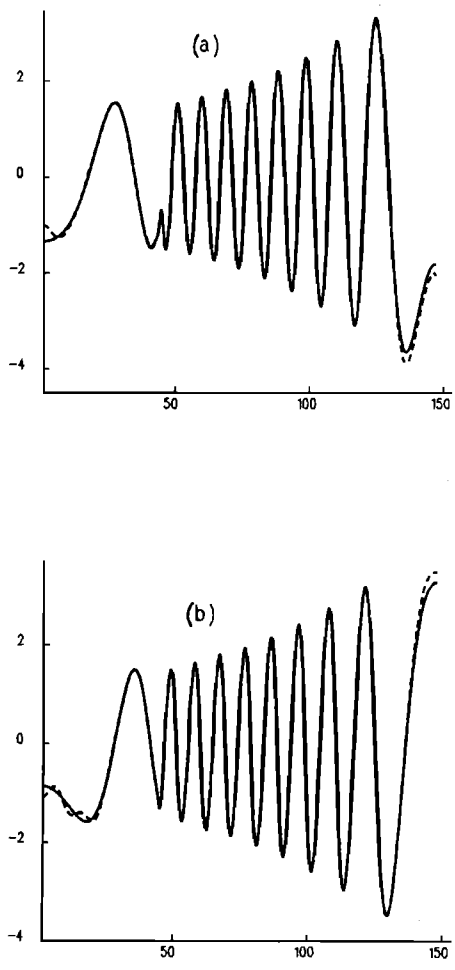

FIG. 14. Same as Fig. 13. O.P.S. check. The mesh satisfies the $\lambda/4$ criterion on the whole surface. — Exact $p(\mathbf{r})$; - - - computed $p(\mathbf{r})$ with $NE = 20$.

Figure 13 shows that the high-frequency approximation usually made for the surface pressure,[39,40]

$$p(\mathbf{r}) = \rho c v(\mathbf{r}) + O(k^{-1}), \quad \mathbf{r} \in S, \tag{43}$$

is not verified here because (i) the surface velocity is discontinuous[41] and (ii) the cylinder possesses two circular wedges: "Diffracted rays," issuing from the discontinuities at $z = \pm z_0 = \pm 0.0365$ m of the surface velocity and from the wedges, induce contributions to (43) of the order of $k^{-1/2}$ for points such as $\rho = a$, $z \neq \pm z_0$ and $\rho = 0$, $z = \pm b$.[42,43] Moreover, the laws of geometrical acoustics ensure that the diffracted rays issuing from $z = \pm z_0$ are asymptotically of the form

$$(A e^{ik(z \mp z_0)}/\sqrt{z \mp z_0}) \rho c v(\pm z_0) \tag{44}$$

for points such as $\rho = a$, $|z_0| < |z| < |b|$, where A is some "diffraction" coefficient of the order of $k^{-1/2}$. We have indeed verified from our numerical results that $p(\mathbf{r}')/p(\mathbf{r})$, with $\mathbf{r} = (\rho = a,\ z_0 < z < b)$, $\mathbf{r}' = (\rho = a,\ z_0 < z' < b)$, verifies (44) with a few percent error.

In order to test the ability of the approximation $p(\mathbf{r}) = \rho c v(\mathbf{r})$, $\mathbf{r} \in S$, to give the correct farfield pattern, we have represented in Figs. 15–17, $20 \log |f_0(\theta)|$, where $f_0(\theta)$ is computed either directly from (40) and (15) [$f_0^c(\theta)$] or approximately from (15) and $p(\mathbf{r}) = \rho c v(\mathbf{r})$ [$f_0^A(\theta)$] for three arrays of radius $a = 0.2665$ m and of semiheight $b = 0.6295$ m, $b = 0.333$ m, and $b = z_0$ (the array is then reduced to its radiating zone). A straightforward calculation gives for $f_0^A(\theta)$:

$$f_0^A(\theta) = -kaz_0\rho c \begin{cases} j_0(kz_0 \cos\theta)[\sin\theta J_1(ak\sin\theta) + iJ_0(ak\sin\theta)], & \theta \neq \pi/2, \\ J_1(ak) + iJ_0(ak), & \theta = \pi/2, \end{cases}$$

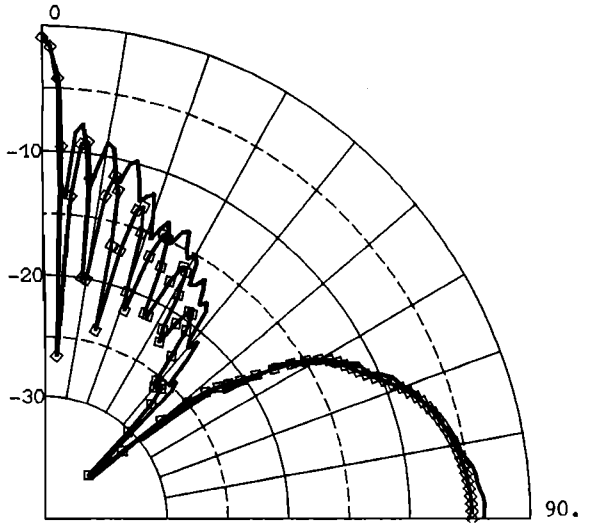

FIG. 15. Directivity pattern in dB computed for the radiating array described in Fig. 13. $\theta = 0°$ is the direction of the revolution axis. The zero level corresponds to 113 dB. — $20 \log |f_0^c(\theta)|$; ⊟ $20 \log |f_0^A(\theta)|$.

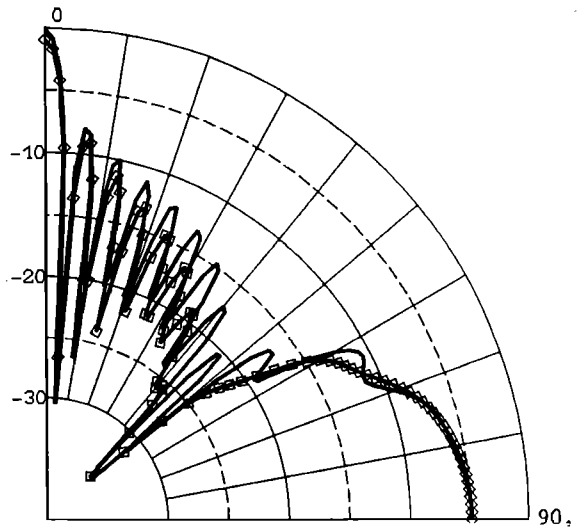

FIG. 17. Same as Fig. 15, but for the cylinder as 0.2665, $b = 0.0365$ [the array is reduced to the radiating zone, which remains unchanged, as well as $f_0^A(\theta)$]. The zero level corresponds to 113 dB.

where $J_n(x)$ is the Bessel function of order n. We see that the main discrepancies between $|f_0^C(\theta)|$ and $|f_0^A(\theta)|$ are localized in the secondary lobes, the best agreement being obtained for the nonbaffled array ($b = z_0$). On the whole, the two calculations are in good agreement: This result is of some importance since the total computing time necessary to obtain f_0^C for the large cylinder is 9500 s (2000 s for the null-field part)!

IV. CONCLUSIONS

The numerical examples presented in this work show that Jones' method is efficient and largely superior to the null-field technique which, as we have shown and for numerical reasons, cannot be used to solve the Helmholtz equation for radiating or scattering objects of high aspect ratio and/or in the high-frequency range. From simple considerations, we have specified the numerical limitations of Jones' method and clarified the role of the additional null-field equations, which has allowed us to perform accurate high-frequency computations at the cost, however, of large computing times, only a small part of which (10%–20%) being devoted to the numerical implementation of the additional equations. It is well known that such a technique is not particularly well suited to the high-frequency range where it is more advisable to use asymptotic methods to compute the directivity pattern, such as the geometrical theory of diffraction (see, e.g., Refs. 42 and 43) or the crude approximation $p(\mathbf{r}) = \rho c v(\mathbf{r})$ used in the preceding section: However, it may be of some help to check the efficiency of such asymptotic methods. Besides, when one wants to solve the radiation or diffraction problem for a complex transducer, the overall dimensions of which are large compared with the wavelength, then the knowledge of the surface impedance is needed in order to perform a finite–element modeling of the device and, for lack of a reliable asymptotic expression of this impedance, the coupled integral equation–null-field method can be used.

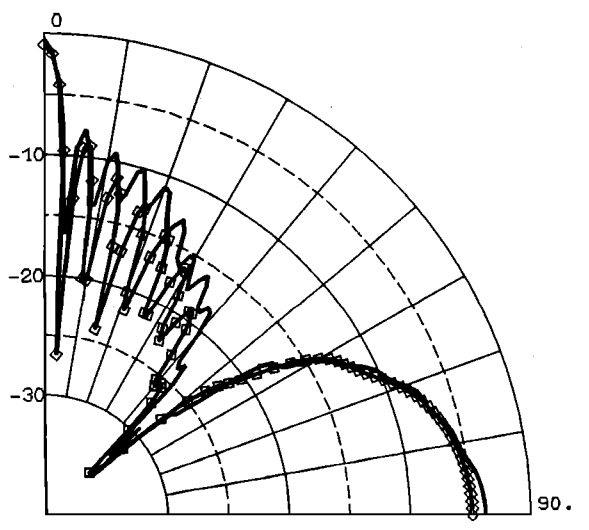

FIG. 16. Same as Fig. 15, but for the cylinder $a = 0.2665$, $b = 0.333$. The radiating zone is unchanged, as well as the values of $f_0^A(\theta)$. The zero level corresponds to 113 dB.

The implementation of the numerical program described here involves no major difficulty, mainly because the solution of the integral equation we use is relatively simple. As it stands, it can be coupled with a finite-element code using the same interpolation functions to represent the object surface and the surface pressure and normal velocity, such as ATILA, and, at least from a formal point of view, there is no difficulty about the extension of this program to the solution of nonaxially symmetrical problems. This point, as well as the coupling with ATILA, is currently under study.

The method presented here is open to further improvements. First, other wavefunctions, solution of the Helmholtz equation in a coordinate system better suited to the shape of the radiating or scattering object, could be used in place of the spherical wavefunctions, provided that their numerical computation is accurate and does not involve too many difficulties. Second, it would be interesting to get some informa-

tion on the general properties of the interior Dirichlet problem eigenfunctions for surfaces of arbitrary shape in order to use R2 with full efficiency. And finally, the following idea[44] could be used: Several simultaneous and finite sets of additional null-field equations could be written at points chosen in the interior volume. Following R2, we may expect then a reduction of the order of the wavefunctions to be used in each set and, hence, to counterbalance the undesirable behavior of these functions for high orders. Note that the implementation of this idea may also improve the efficiency of the null-field method.

ACKNOWLEDGMENTS

The numerical implementation of the null-field equations was greatly aided by the immediate availability of a very accurate and reliable program for computing the spherical Hankel functions, which had been developed by R. Bossut and G. Allan. We are also grateful to them for the helpful advice they gave us concerning the numerical and software aspects of this work. A part of this work has been performed under contract with the Groupe d'Etude et de Recherche en Détection Sous-Marine (GERDSM, DCAN Toulon, France), which is gratefully acknowledged.

APPENDIX A

These assertions may be established more rigorously. For M sufficiently large, we have, from (30) and (31),

$$\left(\frac{2M+1}{e}\right)^M \int_0^\pi g(\theta) e^{(M+1)h(\theta)}\, d\theta \sim 0, \tag{A1}$$

with

$$g(\theta) = -(i/\sqrt{2e})\epsilon(r(\theta)) P_{M-1}(\cos\theta) \times w(\theta)\partial n(kr(\theta)),$$

$$d\mathbf{r} = w(\theta)d\theta,$$

$$h(\theta) = -\operatorname{Log} kr(\theta).$$

The major contribution to the value of the integral arises from the immediate vicinity of those points of the interval $0 \leqslant \theta \leqslant \pi$ at which $h(\theta)$ assumes its largest value. Let us call $\theta_{\min}$ one of these points for which $r = r_{\min}$; then, following Ref. 45, (A1) is equivalent to

$$\frac{b}{\nu}\Gamma\left(\frac{\lambda}{\nu}\right)\left(\frac{\nu}{a(M+1)}\right)^{\lambda/\nu} \frac{(2M+1)^M \epsilon(r_{\min})}{e^M (kr_{\min})^{M+1}} \sim 0,$$

where $a, \lambda > 0$ and $\nu > 0$ are defined by

$$\frac{dh(\theta)}{d\theta} \sim -a(\theta - \theta_{\min})^{\nu-1}, \quad \theta \to \theta_{\min} + 0,$$

$$g(\theta) \sim b\epsilon(r_{\min})(\theta - \theta_{\min})^{\lambda-1}, \quad \theta \to \theta_{\min} + 0.$$

Hence, for a sufficiently large M, there is a $\eta > 0$ so that

$$|\epsilon(r_{\min})| < \eta \frac{kr_{\min}}{|(b/\nu)\Gamma(\lambda/\nu)|} \times \left(\frac{a(M+1)}{\nu}\right)^{\lambda/\nu} \left(\frac{ekr_{\min}}{2M+1}\right)^M,$$

and $\lim_{M\infty} \epsilon(r_{\min}) = 0$.

The arguments developed above show (i) that the part Δ of the surface S on which $p(\mathbf{r})$ is accurately computed starts at $r = r_{\min}$, (ii) that the value of M from which this phenomenon occurs is roughly proportional to $kr_{\min}$ (see above inequality), and (iii), if repeated for possible relative minima, the arguments suggest that such zones Δ will appear at these minima for still larger values of M.

APPENDIX B

When $l = j$, it is advisable to isolate the singular part of the integrands in $A^j_{j\alpha}$, $B^j_{j\alpha}$, and to integrate it separately. Hence, we write

$$\operatorname{Re} A^j_{j\alpha}(\zeta) \equiv \operatorname{Re} A(\zeta) = -\frac{1}{2\pi}\int_0^\pi \left(\frac{\cos[kd(\zeta,\varphi)] - 1}{d(\zeta,\varphi)} + k\sin[kd(\zeta,\varphi)]\right)\frac{[\mathbf{r}'(\zeta,\varphi) - \mathbf{r}_{j\alpha}]\cdot\mathbf{n}'}{d^2(\zeta,\varphi)}\, d\varphi + A'(\zeta),$$

$$A'(\zeta) = -\frac{1}{2\pi}\int_0^\pi \frac{[\mathbf{r}'(\zeta,\varphi) - \mathbf{r}_{j\alpha}]\cdot\mathbf{n}'}{d^3(\zeta,\varphi)}\, d\varphi,$$

and

$$\operatorname{Re} B^j_{j\alpha}(\zeta) \equiv \operatorname{Re} B(\zeta) = \frac{1}{2\pi}\int_0^\pi \frac{\cos[kd(\zeta,\varphi)] - 1}{d(\zeta,\varphi)}\, d\varphi + B'(\zeta),$$

$$B'(\zeta) = \frac{1}{2\pi}\int_0^\pi \frac{d\varphi}{d(\zeta,\varphi)}.$$

Because of axial symmetry, $A'(\zeta)$ and $B'(\zeta)$ can be recognized as complete elliptic integrals, or sums of such integrals, and calculated through the approximations given in Ref. 46. The imaginary parts of $A(\zeta)$ and $B(\zeta)$ are computed with the Gauss–Legendre quadrature rule.

APPENDIX C

If S_i is the sphere of radius R_i lying entirely within S, then, from (8) and (12), we have

$$\eta(\mathbf{r}) = ik\sum_{m=0}^{\infty}\sum_{|n|\leqslant m} A_{nm}\overline{\Psi}^n_m(\mathbf{r}), \quad r < R_i,$$

$$A_{nm} = \int_S u(\mathbf{r}')\partial n'\, \Psi^n_m(\mathbf{r}')d\mathbf{r}',$$

where $u(S)$ satisfies (7), i.e., is a solution to the homogeneous equation associated with (4) for a given irregular frequency. Then $u(S)$ satisfies (9) where the right-hand side of (9) is zero, which corresponds to $A_{nm} = 0$ for $0 \leqslant m \leqslant M-1$, $|n| \leqslant m$. Thus,

$$\eta(\mathbf{r}) = ik\sum_{m=M}^{\infty}\sum_{|n|\leqslant m} A_{nm}\overline{\Psi}^n_m(\mathbf{r}), \quad r < R_i. \tag{C1}$$

First, let us assume that we have axial symmetry ($n = 0$). Then, from (13), we have, in the vicinity of the origin,

$$\eta(\mathbf{r}) \underset{r\to 0}{\sim} \frac{ik\sqrt{\pi}(kr)^M}{(M+1/2)!2^{M+1}} \times A_{0M} Y^0_M(\theta) + O[(kr)^{M+1}], \tag{C2}$$

so that $\eta(\mathbf{r})$ behaves for small r like $Y_M^0(\theta)$. More rigorously, we look for the locus of the points where $\eta = 0$ for small r. If we apply to (C1) the arguments given in Ref. 47, then we obtain R2, and the nodal surfaces of η will divide V_i into at least $(M+1)$ subdomains, $Y_M^0(\theta)$ having M nodal surfaces, and $\eta(S) = 0$. If $n \leqslant M$ is the number of the eigenvalue of (6) associated with the eigenfunction η, then, from Ref. 37, η cannot divide V_i in more than n subdomains. Since this contradicts the previous result, η is identically zero inside S_i and, from (C1) and the orthogonality of the Y_m^n, $A_{0m}\, j_m(kr) = 0$ for all m. Choosing r so that kr is not a zero of $j_m(kr)$, this implies $A_{0m} = 0$ for all m and, from the definition of the A_{nm} and the completeness on S of $\{\partial n\, \bar{\Psi}_m^n\}$, $u(S) = 0$: this proves R1.

For a non-axially-symmetric problem, the same arguments can be resumed, and, in particular, (C2) is obtained if we prescribe

$$A_{nm} = 0, \quad 0 \leqslant m \leqslant M-1, \quad |n| \leqslant m,$$
$$A_{nM} = 0, \quad \text{for all } n \neq 0,$$

which corresponds to

$$\int_S p(\mathbf{r}) \partial n\, \Psi_m^n(\mathbf{r}) d\mathbf{r} = \int_S \partial n\, p(\mathbf{r}) \Psi_m^n(\mathbf{r}) d\mathbf{r}, \quad 0 \leqslant m \leqslant M-1, \quad |n| \leqslant m,$$

$$\int_S p(\mathbf{r}) \partial n\, \Psi_M^n(\mathbf{r}) d\mathbf{r} = \int \partial n\, p(\mathbf{r}) \Psi_M^n(\mathbf{r}) d\mathbf{r}, \quad \text{for all } n \neq 0, \quad |n| \leqslant M.$$

In this case, the behavior of η in the vicinity of the origin is also given by R2, and, at least, the M first irregular frequencies are eliminated.

[1]O. C. Zienkiewicz and R. E. Newton, Proceedings of the Symposium on Finite Element Techniques, Stuttgart, 1969.
[2]D. V. Dean, Ph.D. thesis, Naval Postgraduate School, Monterey, CA, 1970.
[3]J. T. Hunt, M. R. Knittel, and D. Barach, J. Acoust. Soc. Am. **55**, 269 (1974).
[4]J. N. Decarpigny, Thèse d'Etat, Université des Sciences et Techniques de Lille, France, 1984.
[5]J. N. Decarpigny, J. C. Debus, and D. Boucher, J. Acoust. Soc. Am. **78**, 1499 (1985).
[6]B. Hamonic, R. Bossut, J. C. Debus, J. N. Decarpigny, D. Morel, P. Tierce, B. Tocquet, and D. Boucher, 11th Seminar on Modal Analysis, Leuven, Belgium, 1986.
[7]P. M. Morse and H. Feshbach, *Methods of Theoretical Physics* (McGraw-Hill, New York, 1953).
[8]R. F. Millar, Radio Sci. **8**, 785–796 (1973).
[9]J. L. Butler, J. Acoust. Soc. Am. **48**, 325–336 (1970).
[10]P. C. Waterman, J. Acoust. Soc. Am. **45**, 1417–1429 (1969).
[11]P. C. Waterman, Phys. Rev. D **3**, 825–839 (1971).
[12]G. Kristensson and P. C. Waterman, J. Acoust. Soc. Am. **72**, 1612–1625 (1982).
[13]V. K. Varadan, V. V. Varadan, S. J. Tsao, and W. G. Neubauer, J. Acoust. Soc. Am. **72**, 1957–1964 (1982).
[14]P. C. Waterman, Proc. IEEE **53**, 805–812 (1965).
[15]J. C. Bolomey and W. Tabbara, IEEE Trans. Antennas Propag. **AP-21**, 356–363 (1973).
[16]W. Tobocman, J. Acoust. Soc. Am. **77**, 369–374 (1985).
[17]D. Colton and R. Kress, *Integral Equation Methods in Scattering Theory* (Wiley, New York, 1983).
[18]A. J. Burton and G. F. Miller, Proc. R. Soc. London Ser. A **323**, 201–210 (1971).
[19]W. L. Meyer, W. A. Bell, B. T. Zinn, and M. P. Stallybrass, J. Sound Vib. **59**, 245–262 (1978).
[20]T. Terai, J. Sound Vib. **69**, 71–100 (1980).
[21]M. N. Sayhi, Y. Ousset, and G. Verchery, J. Sound Vib. **74**, 187–204 (1981).
[22]H. A. Schenck, J. Acoust. Soc. Am. **44**, 41–58 (1968).
[23]R. Courant and D. Hilbert, *Methods of Mathematical Physics* (Interscience, New York, 1953), 1st ed., Vol. 1, p. 442.
[24]G. Chertock, Naval Ship and Research Development Center, Washington DC, Report No. 3538, 1971.
[25]W. Tobocman, J. Acoust. Soc. Am. **80**, 1828–1837 (1986).
[26]A. F. Seybert and T. K. Rengarajan, J. Acoust. Soc. Am. **81**, 1299–1306 (1987).
[27]D. S. Jones, Q. J. Mech. Appl. Math. **XXVII**, 129–142 (1974).
[28]Reference 23, Vol. 1, pp. 408–409.
[29]T. S. Angell and R. E. Kleinman, SIAM J. Math. Anal. **16**, 259–278 (1985).
[30]R. E. Kleinman, G. F. Roach, and S. E. G. Strom, Proc. R. Soc. London Ser. A **394**, 121–136 (1984).
[31]J. C. Bolomey and A. Wirgin, Proc. IEE **121**, 794–804 (1974).
[32]R. F. Millar, IMA J. Appl. Math. **30**, 27–37 (1983).
[33]R. H. Hackman, J. Acoust. Soc. Am. **75**, 35–45 (1984).
[34]M. F. Iskander, P. W. Barber, C. H. Durney, and H. Massoudi, IEEE Trans. Microwave Theory Tech. **28**, 801–807 (1980).
[35]A. F. Seybert, B. Soenarko, F. J. Rizzo, and D. J. Shippy, J. Acoust. Soc. Am. **77**, 362–368 (1985).
[36]A. F. Seybert, B. Soenarko, F. J. Rizzo, and D. J. Shippy, J. Acoust. Soc. Am. **80**, 1241–1247 (1986).
[37]Reference 23, Vol. 1, p. 452.
[38]F. Ursell, Proc. Cambridge Philos. Soc. **84**, 545–548 (1978).
[39]G. Chertock, J. Acoust. Soc. Am. **47**, 387–388 (1970).
[40]C. A. Felippa, J. Appl. Mech. **47**, 703–708 (1980).
[41]M. Lax and F. Feshbach, J. Acoust. Soc. Am. **19**, 682–690 (1947).
[42]J. B. Keller, Bull. Am. Math. Soc. **84**, 727–750 (1978).
[43]J. B. Keller, J. Appl. Phys. **28**, 426–444 (1957).
[44]P. Filippi (private communication).
[45]A. Erdélyi, *Asymptotic Expansions* (Dover, New York, 1956), pp. 36–37.
[46]M. Abramovitz and I. Stegun, *Handbook of Mathematical Functions* (Dover, New York, 1972), pp. 591–592.
[47]O. D. Kellogg, *Foundations of Potential Theory* (Springer, New York, 1967), 1st ed., pp. 273–275.